PAPER • **OPEN ACCESS**

Optimizing magnetic hyperthermia for melanoma: the role of nanoparticle uptake inhibition

To cite this article: Beatriz T Simões *et al* 2025 *Nano Ex.* **6** 015017

IOP Publishing Nano Express 6 (2025) 015017 https://doi.org/10.1088/2632-959X/adbde1

NANO EXPRESS

PAPER

Optimizing magnetic hyperthermia for melanoma: the role of nanoparticle uptake inhibition

Beatriz T Simões[1,2], **Catarina Chaparro**[1,2], **Tânia Vieira**[3], **Manuel A Valente**[4], **Marco C V Cavaco**[2], **Vera Neves**[2], **Jorge C Silva**[3], **João Paulo Borges**[1], **Filipe V Almeida**[1] **and Paula Soares**[1]

[1] CENIMATli3N, Department of Materials Science, NOVA School of Science and Technology, NOVA University Lisbon, Caparica, Portugal
[2] Instituto de Medicina Molecular João Lobo Antunes, Lisbon, Portugal
[3] CENIMATli3N, Department of Physics, NOVA School of Science and Technology, NOVA University Lisbon, Caparica, Portugal
[4] Physics Departmentli3N, University of Aveiro, Campus Universitário de Santiago, Aveiro, Portugal

E-mail: pi.soares@fct.unl.pt

Keywords: iron oxide nanoparticles, magnetic hyperthermia, melanoma cells, small-molecule inhibitors

Supplementary material for this article is available online

OPEN ACCESS

RECEIVED
9 January 2025

REVISED
27 February 2025

ACCEPTED FOR PUBLICATION
7 March 2025

PUBLISHED
20 March 2025

Abstract

Superparamagnetic iron oxide nanoparticles (SPIONs) are widely used in magnetic hyperthermia, where their therapeutic efficacy depends on efficient heat generation. However, intracellular uptake of SPIONs has been shown to reduce their heat dissipation capacity, limiting hyperthermia performance. To address this challenge, we explored the use of small-molecule endocytosis inhibitors to block SPIONs' uptake *in vitro*. SPIONs stabilized with 3-aminopropyl triethoxysilane (APTES) were evaluated in an advanced cutaneous melanoma cell line treated with a small library of endocytosis inhibitors. Among these, methyl-β-cyclodextrin significantly reduced SPIONs' uptake compared to untreated cells. Importantly, uptake inhibition restored SPIONs' heat dissipation capacity from specific absorption rates of 63 to 91 W g^{-1} and improved the temperature increase by 2.6 °C, under magnetic hyperthermia conditions. These findings demonstrate that targeting nanoparticle internalization with small-molecule inhibitors, particularly methyl-β-cyclodextrin, enhances the efficiency of magnetic hyperthermia in melanoma cells. This strategy offers a promising approach to optimize magnetic hyperthermia for melanoma treatment.

1. Introduction

Despite advancements in medical science, cancer persists as a global public health challenge, evidenced by its increasing prevalence and mortality rates [1]. Cutaneous melanoma, the most lethal type of skin cancer, registered a worldwide total of 331 k new cases in 2022, which is expected to increase in 2040 by 50% [2, 3]. While associated with risk factors such as age, race, and gender, melanoma arises from several genetic mutations in melanocytes, primarily triggered by overexposure to UV radiation [4, 5]. Nowadays, early-stage melanoma is highly treatable through a combination of tumor removal and radiotherapy to prevent recurrence. In addition, significant efforts have been directed toward developing effective therapeutics for advanced cutaneous melanoma based on targeted and immunotherapy approaches [6]. Immune checkpoint inhibitors and small-molecule targeted drugs, individually or in combination, have demonstrated the potential to enhance patient quality of life [7, 8]. However, melanoma drug resistance, limited response rates, and associated toxicity effects lead to recurrence and disease progression over time [9–12]. So, there is an urgent need to find alternative drug-independent interventions.

The rapid advances in nanotechnology and the unique features of bionanomaterials have prompted new approaches to develop and improve cancer therapies. Superparamagnetic iron oxide nanoparticles (SPIONs) have been the focus of many researchers as potential multifunctional systems comprising drug delivery properties, image contrast, and magnetic hyperthermia agents [13–16]. At the nanometric scale, typically below

20 nm for iron oxide, the nanoparticles exhibit superparamagnetic behaviour, which translates into the ability to exhibit magnetic properties only when a magnetic field is applied, showing great promise in the biomedical field [17]. In an effort to overcome the limitations associated with the clinical applicability of local hyperthermia, magnetic hyperthermia has emerged as a new non-invasive modality, achieving targeted heat production with SPIONs [18]. With the application of an alternating magnetic field (AMF) that is highly penetrable into the human body, SPIONs accumulated at a tumor site can dissipate heat. This aims to induce apoptosis in malignant cells due to their temperature susceptibility while leaving surrounding tissue unharmed [16, 19]. However, SPIONs capacity to dissipate heat can be affected by several factors.

Recent studies have shown that the dynamic magnetic response of SPIONs inside cells can drastically change [20–22]. Hannon *et al* (2020) *in vitro* study in a pancreatic cell line reported that SPIONs magnetic heating efficiency reduces upon internalization, lowering the levels of cell death [23]. Although the mechanisms behind this phenomenon are not fully defined, it is suggested that it may be due to particle immobilization, nanoparticle clustering, or the influence of the medium viscosity. What appears to be consistent in the literature is that hyperthermia appears to be therapeutically more effective when SPIONs are in the extracellular environment [20, 24, 25].

Here, we explore a novel approach to enhancing magnetic hyperthermia for melanoma treatment by impairing the cellular internalization of SPIONs. Since endocytosis is the predominant internalization pathway for various nanoparticles, we utilized small molecule endocytosis inhibitors (SMIs) to reduce SPION uptake. As a proof of concept, we selected five well-characterized SMIs that target distinct endocytic pathways: chlorpromazine (CPZ), genistein, methyl-β-cyclodextrin (MβCD), nocodazole, and latrunculin B [26–30]. With this approach, we aim to compare the heating capacity of SPIONs in intracellular hyperthermia (when internalized) against extracellular hyperthermia (when internalization is impaired) conditions. To our knowledge, no report combines small molecule inhibitors of endocytosis to improve magnetic hyperthermia therapy.

2. Materials and methods

2.1. Materials

The chemicals 3-aminopropyl) triethoxysilane (APTES), *N*-(3-dimethylaminopropyl)-*N*′-ethylcarbodiimide hydrochloride) (EDC.HCl), *N*-hydroxysuccinimide (NHS), rhodamine B (RhoB), and 2-(*N*-morpholino) ethanesulfonic acid (MES) were all purchased from Merck. The selected SMI for the present work were CPZ (Target Molecule), genistein (Target Molecule), latrunculin B (Focus Biomolecules), nocodazole (Cayman Chemical) and MβCD (Cayman Chemical). For cytotoxicity studies, the following reagents were used: resazurin sodium salt from Alfa Aesar; Calcein AM (green dye live cell indicator), and ethidium homodimer (red dye dead cell indicator) from Biotium. For immunostaining studies, the following reagents were used: paraformaldehyde (PFA) (Merck), triton-X-100 (Omnipur), bovine serum albumin (BSA) (Sigma-Aldrich) and Mowiol 4–88 mounting medium (Sigma-Aldrich), Helix NPTM 488 dye (Biolegend) and Actin-staining PhalloidinTM 488 dye (Cytoskeleton). For Prussian blue staining: Perl's reagent was used containing 4% potassium hexacyanoferrate (II) trihydrate, $K_4[Fe(CN)_6].3H_2O$ (w/v), and 4% HCl (v/v); counterstaining solution used was Nuclear fast red 0.1% in 5% aluminum sulfate, all from Sigma-Aldrich.

2.2. Synthesis and stabilization of magnetic nanoparticles

SPIONs were synthesized by chemical co-precipitation technique following the procedure described in Soares *et al* [31]. The resultant nanoparticle suspension was stabilized with APTES surfactant, following the Mashhadizadeh *et al* [32] protocol. Briefly, bare SPIONs produced by co-precipitation were dispersed in a 10% (v/v) solution of APTES prepared in a 1:2 mixture of ultrapure water and glycerol. The reaction was left to proceed at 90 °C under mechanical stirring for 2 h. After cooling to room temperature, the suspension was washed five times by magnetic separation, alternating between water and ethanol, and stored in water at 4 °C. For further studies using fluorescence microscopy, the obtained APTES stabilized SPIONs were functionalized with RhoB fluorophore via EDC/NHS coupling in a proportion of 2 mM RhoB to 1.5 mg ml^{-1} SPIONs resuspended in MES buffer. The nanoparticles concentration in the colloidal solution was determined in iron content using the 1,10-phenanthroline colorimetric method, considering [Fe] = 0.7 × [SPIONs] [33].

2.3. Characterization of magnetic nanoparticles

SPIONs were characterized in terms of chemical composition by Fourier transform infrared (FTIR), x-ray diffraction (XRD), and morphology by Transmission Electron Microscopy (TEM), before and after APTES stabilization. For XRD and FTIR analysis, all nanoparticles were freeze-dried for 48 h. XRD analysis was performed in a X'Pert PRO MDP x-ray diffractometer (PANalytical), employing Cu-Kα radiation

(k = 1.54060 Å). The analysis spanned a range of 2θ values between 15° and 80° with a step of 0.033°. FTIR spectra were acquired using FTIR Nicolet 6700 (Thermo Electron Corporation) with attenuated total reflectance with a 45° incident angle in the 4500 –500 cm^{-1} range. TEM images were obtained with a Hitachi H-8100 II with thermionic emission LaB6. The SPIONs size distribution was determined using ImageJ software [34].

Prior to *in-vitro* studies, SPIONs stability in serum and protein corona formation was observed by Dynamic Light Scattering (DLS) and ζ-potential analysis. SPIONs were dispersed in a cell culture medium with 0% and 10% FBS and water at pH 7 and left to incubate at 37 °C for 24 h. The hydrodynamic size (Dh) and surface charge were measured for 0.05 mg ml^{-1} of SPIONs at a scattering angle of 90 °C using a SZ-100 nanopartica series with a 532 nm laser containing a Peltier system at 25 °C. The Dh was calculated using the Stokes–Einstein equation. Magnetic properties of SPIONs were measured through Vibrating Sample Magnetometer (VSM) technique using a 10 T VSM magnetometer (Cryogenic-Cryofree). The magnetization curve was obtained at 5 K and 300 K, with a variation of the applied field of −5 T up to 5 T.

2.4. In-vitro cell culture

WM983b cell line of metastatic cutaneous melanoma cancer was provided by Rockland Immunochemicals Inc. (WM983B-01-0001). This cell line was cultivated in Dulbecco's modified Eagle's medium (DMEM) high glucose (4.5g l^{-1}), supplemented with 5% heat-inactivated fetal bovine serum (FBS) and 1% penicillin–streptomycin antibiotic, all from Biowest. For spheroid culture, 1.5% Agar solution (Sigma-Aldrich) dissolved in phosphate buffer saline (PBS) solution and collagen type-I rat tail (Sigma-Aldrich) were used. Cells were grown in an MCO-19AIC(UV) CO_2 incubator with a humidified atmosphere of 5% CO_2 at 37 °C, with the medium changed every other day.

For all *in-vitro* experiments, SPIONs were diluted in WM983b culture medium containing 10 μg ml^{-1} gentamicin antibiotic (Gibco). CPZ, genistein, latrunculin B, and nocodazole were dissolved in dimethyl sulfoxide (DMSO) and diluted in a cell culture medium containing 1% DMSO in the final solution. MβCD was dissolved in WM983b culture medium directly and syringe filtered for sterilization.

2.4.1. Cytotoxicity studies

The potential cytotoxic effects of SPIONs towards WM983b cell line was assessed by Live/Dead cell viability test, using Live/Dead solution, containing 0.2 μl ml^{-1} Calcein AM and 0.8 μl ml^{-1} Ethidium homodimer, prepared in serum-free WM983b culture media with 25 mM of 4-(2-hydroxyethyl)-1-piperazine ethane sulfonic acid (HEPES). Briefly, WM983b cells were seeded in a 96-well plate at 150 kcell ml^{-1} and incubated with a range of SPIONs concentrations from 0.06 mg ml^{-1} to 1 mg ml^{-1} diluted in medium containing 10 μg ml^{-1} gentamicin. After 24 h of SPIONs exposure, cells were incubated with Live/Dead solution for 30 min. Reaction was stop by washing with medium containing serum. The percentage of live and dead cells was obtained through image analysis, given by [Cell viability (%) = cell count/untreated control cell count × 100]. Outliers were removed considering a 0.05 significance level. At least 10 images of each condition were taken by epifluorescence microscopy using a Nikon Inverted microscope with 10 × magnification.

The toxicity of the SMIs was determined by resazurin-based cell viability assay. Similar to SPIONs viability assay, WM983b cells were seeded in a 96-well plate at 150 kcell ml^{-1} and incubated for 24 h with a range of concentrations of CPZ, genistein, latrunculin B, nocodazole, and MβCD. After treatment, 20 μg ml^{-1} resazurin solution was added for 2 h. The change in absorbance between 570—600 nm wavelength was measured using BioTek ELx800 UV absorbance microplate reader. The quantity of viable cells was determined by the measured absorbance related to the absorbance of the respective control (cells untreated with SMI). Cell viability was expressed as a percentage of the control, given by [Cell viability (%) (Abs_{570}—Abs_{600}) treated cells/(Abs570—Abs600) untreated control × 100].

2.4.2. Cellular uptake studies: prussian blue staining

The dynamic interaction of SPIONs with WM983b cells was evaluated with Prussian blue staining in different in vitro models: single-cell suspension, cell monolayer (2D model), and cell spheroid (3D model).

To obtain a single-cell suspension, 100 kcell ml^{-1} of WM983b cells were seeded simultaneously with SPIONs, in a 6-well plate and incubated under mild agitation. Cells were left to adhere in 12 mm coverslips for 24 h for imaging acquisitions. A cell monolayer was obtained with 300 kcell ml^{-1} seeding density of WM983b cells in 12 mm coverslips in 24-well plate. Cells were left to adhere in 12 mm coverslips for 24 h before treatment with SPIONs. Spheroids were prepared by seeding 5 kcell $well^{-1}$ in a 96-well plate previously coated with 50 μl $well^{-1}$ of 1.5% agar solution prepared in PBS. After 7 days, SPIONs were added to fully grown spheroids. The same 100 μg ml^{-1} of SPIONs was used for all models with incubation periods of 15 min, 1 h, 3 h, 6 h and 24 h.

To stain the iron content, cells were fixed with 4% PFA for 10 min, permeabilized with 0.2% Triton-X 100 for 30 min, and stained with Perl's reagent and Nuclear fast red for 40 min. This procedure was done in

coverslips for single-cell suspension and cell monolayer models; spheroids were previously embedded in 2 mg ml^{-1} collagen type-I rat tail matrix. At least 10 images of each condition were acquired with Nikon Ti-S Inverted Microscope in phase contrast mode using a 20 × objective magnification. Antifade Mowiol mounting medium was used for sample preservation, prepared as recommended [35].

2.4.3. Cellular uptake studies: fluorescence microscopy

As a complementary approach using a higher resolution imaging technique, Laser Scanning Confocal microscopy was used. WM983b cell monolayer, obtained as described above, was exposed to 100 μg ml^{-1} of RhoB functionalized SPIONs for 1 h. To reduce background and facilitate observation of SPIONs localization within the cell, the excess of non-internalized SPIONs was removed by rinsing the cells with medium, following additional 1 h, 3 h, 6 h, 16 h and 24 h incubation periods.

For imaging acquisition, cells were fixed in the coverslips with a 4% PFA solution for 10 min, and permeabilized with 0.2% Triton-X 100 for 20 min. Nuclear and cytoskeleton stainings were performed with Helix NP^{TM} 488 (1:1000 from a stock of 5 mM) and Actin-staining Phalloidin^{TM} 488 (100 nM), diluted in 0.2% BSA solution, for 30 min. Antifade Mowiol mounting medium was used for sample preservation, prepared as recommended [35]. At least 10 images of each condition were acquired with a Zeiss LSM 700 microscope, with 488 nm and 555 nm laser lines, in Z-stack mode, using a 20 × objective.

2.4.4. Evaluation of small-molecule inhibitors blocking capacity

The efficiency of the SMI in inhibiting SPIONs internalization was assessed by Laser Scanning Confocal microscopy. WM983b cells were seeded in 12 mm coverslips in 24 well-plate at 100 kcell ml^{-1} for 24 h. 1 h pre-treatment with each SMI (25 μM genistein, 5 μM CPZ, 10 μM latrunculin B, 5 mM MβCD and 10 μM nocodazole) was followed. Then, 100 μg ml^{-1} of RhoB functionalized SPIONs were co-incubated with the SMI for redosing for an additional 6 h. The same above mentioned protocol was executed for confocal microscopy sample preparation.

A quantitative analysis of the images acquired with confocal microscopy was performed to obtain the percentage of SPIONs cellular uptake. Image processing was performed considering individual cells, where each cell area was delimited manually. To account for the SPIONs signal in the cytoplasm, a binary mask of the cell nucleus was obtained by applying an Otsu's threshold to the green channel. To get the SPIONs distribution along the cytoplasm, the identified cell nuclei suffered consecutive iterative dilations by a disc structuring element with 3-pixel width, until all cell area was covered. For each 3-pixel width disc, from the cell nucleus to the cell end, the mean fluorescence intensity of the RhoB functionalized SPIONs red channel was determined and converted to an RGB scale from 0–255. From this analysis, the SPIONs distribution profile in the cell's cytoplasm was obtain from an average of intensity per disc for at least 20 cells per condition. The cellular uptake per cell corresponds to the area under the curve of the SPIONs distribution profile. The percentage of SPIONs cellular uptake was determined as an average of the cellular uptake per cell.

2.4.5. Flow cytometry

WM983b cells were seeded at 50 kcell ml^{-1} in 24-well plate for 24 h. Then, the medium was removed, and cells were rinsed twice with PBS and once with fresh medium. For uptake studies, cells were incubated for 1 h, 6 h, and 24 h with 100 μg ml^{-1} of RhoB functionalized SPIONs. Then, cells were collected and rinsed twice with PBS. The fluorescence intensity of 10 kcell was analyzed with a BD LSRFortessa X-20 flow cytometer. The mean fluorescence of samples was obtained by subtracting the autofluorescence of cells. All experiments were performed in duplicates in three independent assays. For evaluation of SMI blocking capacity, the same protocol was applied, adding 1 h pre-treatment with 5 mM of MβCD before incubation with the SPIONs.

2.5. Magnetic hyperthermia assays

All magnetic hyperthermia assays were performed in DM100 series from nB nanoScale Biomagnetics apparatus. An AMF of 300 G with a frequency of 418.5 kHz was applied for 10 min in all studies unless stated otherwise. Temperature was measured in a sealed glass dewar flask using an optic sensor. SPIONs temperature curves were registered for 1 mg ml^{-1}, 2 mg ml^{-1}, and 3.5 mg ml^{-1} of SPIONs suspension to determine the optimal concentration to reach therapeutic temperatures of 42 °C, within 5 min. Prior to *in-vitro* assays, the influence of WM983b cell culture conditions in the heating capacity of SPIONs was evaluated. For that, SPIONs were dispersed in: water or PBS and incubated for 24 h at 4 °C or 37 °C with a humidified atmosphere of 5% CO_2; or in DMEM cell culture medium with or without FBS and incubated for 24 h at 37 °C with a humidified atmosphere of 5% CO_2. The specific absorption rate (SAR) value characterizes the magnetic colloid heating capacity and was calculated according to [36], approximating the cell culture medium-specific heat to the water-specific heat.

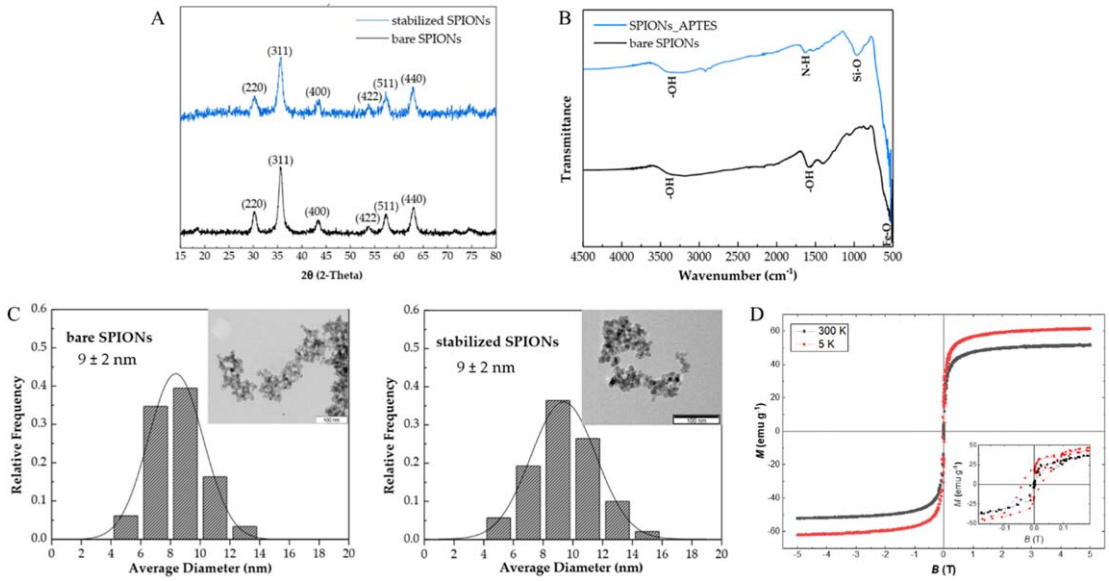

Figure 1. Morphological, chemical, and structural characterization of bare SPIONs and APTES stabilized SPIONs. (A) XRD diffractograms of both bare and APTES stabilized SPIONs, identifying characteristic peaks and respective diffraction planes, were analysed according to the crystallographic sheets of standard XRD pattern. (B) FTIR spectra of both bare and APTES stabilized SPIONs, comparing the presence of specific absorbance bands representative of chemical bonds within the nanoparticles. (C) TEM images of both bare and APTES stabilized SPIONs show the particles' spherical morphology. Size distribution graphics were obtained using Image J program, where bars represent the relative frequency of the diameters, and line represent a Gaussian curve fitting. Scale bar: 100 nm. (D) Magnetization as a function of the applied magnetic field at 5 K and 300 K of SPIONs_APTES. Magnetization values are presented in emu per gram of the whole particle (including magnetic and non-magnetic material).

In vitro magnetic hyperthermia assays were performed with the following conditions: SPIONs uptake inhibition by MβCD, intracellular and extracellular controls. For SPIONs uptake inhibition, 3.5 kcells were pre-treated with 5 mM MβCD for 1 h, following 6 h co-incubation period of 5 mM MβCD and 3.5 mg of SPIONs. The same treatment proportion of 3.5 mg of SPIONs per 3.5 kcells was maintained for all conditions. For intracellular control, SPIONs were incubated for 6 h to reach maximum uptake, whereas for extracellular control SPIONs were added to the cell suspension only at the time of measurement. Magnetic hyperthermia measurements were performed with the cells in suspension.

A summary of the experimental procedures is given in Scheme S1 (Supplementary information).

2.6. Statistical analysis

All data points are presented as mean ± standard deviation (SD). A t-test statistical analysis was applied to the mean values relative to the considered control. The hypothesis test considered samples with different deviations in bimodal distribution. ****p-value < 0.0001 ***p-value < 0.001, **p-value < 0.01, *p-value < 0.05.

3. Results

3.1. SPIONs characterization: XRD, FTIR, and TEM

The diffractograms in figure 1(A), acquired by the XRD technique, reveal a crystalline cubic structure mainly constituted of magnetite for bare SPIONs. This structure remains preserved after stabilization with the APTES molecule. The analysis of the diffractograms was performed according to the crystallographic sheets of standard XRD pattern where six characteristic peaks were identified at 2θ equal to 30.3, 35.6, 43.3, 53.6, 57.2 and 63.1, corresponding to the diffraction planes (2 2 0), (3 1 1), (4 0 0), (4 2 2), (5 1 1) and (4 4 0), respectively [31]. Using Scherrer's equation, the average crystallite size calculated for both bare and APTES stabilized SPIONs was around 9 nm, considering a maximum peak at $2\theta = 35.56$ for bare SPIONs and $2\theta = 35.69$ for SPIONs_APTES [36].

The FTIR spectra of both bare and APTES stabilized SPIONs (figure 1(B)) allow the identification of the sharp absorbance band at 560 cm^{-1} in all spectra, which is related to the stretching vibration mode of the Fe–O bond originating from the SPIONs iron oxide core. The broadband between 3000 cm^{-1} and 3500 cm^{-1} is related to the O–H stretching vibration mode due to hydration water, while the band at 1590 cm^{-1} in the bare SPIONs spectrum is related to the O–H stretching vibration modes. The band that appears around 1630 cm^{-1} in the FTIR spectra of APTES stabilized SPIONs corresponds to the amine bending mode from the APTES amine

Table 1. Comparison between ζ—potential values and Hydrodynamic sizes of SPIONs in different dispersion media. Dh, hydrodynamic size; PDI, polydispersity index. Data is expressed as mean ± SD for at least five measurements.

Sample	Dispersion medium	ζ–potential (mV)	Dh (nm)	PDI
SPIONs_APTES	Water	+30 ± 3	227 ± 3	0.35
	DMEM with 0% FBS	+0.1 ± 1.6	24301 ± 1927	4.70
	DMEM with 10% FBS	−1.6 ± 1.0	23250 ± 1880	5.52
	PBS	−3.6 ± 1.1	30979 ± 4709	24.7
SPIONs_RhoB	Water	−14 ± 2	16792 ± 2663	3.66
	DMEM with 0% FBS	− 1.9 ± 1.1	20822 ± 2802	1.60
	DMEM with 10% FBS	− 2.1 ± 1.0	19486 ± 256	1.18

functional group, whereas the absorbance band around 1100 cm^{-1} is due to the stretching vibration of Si–O [37], confirming of the presence of APTES at SPIONs surface. The functionalization of SPIONs with RhoB fluorophore was also verified by FTIR (Supplementary Information, figure S1A). The absorbance band around 1650 cm^{-1}, attributed to the double bond C=O stretching vibration mode, confirms the formation of an amide functional group, resulting from EDC/NHS coupling between the RhoB carboxylic acid bond and the APTES amine group. The spectrum profile between 1700 cm^{-1} and 500 cm^{-1} and the double bonds C=C stretching vibration mode corresponding to the absorbance band at 1500 cm^{-1} are characteristic of aromatic compounds that compose the RhoB molecule. The stretching vibration mode of the Fe–O bond (sharp band at 560 cm^{-1}) from the iron oxide core as well as the stretching vibration of Si–O (around 1100 cm^{-1}) from the APTES molecule, are also present.

Figure 1(C) shows TEM images of bare and APTES stabilized SPIONs that reveal an average size of 9 ± 2 nm, with a narrow size distribution, within the range with a superparamagnetic behavior (<15 nm) [38]. In general, the presence of APTES at SPIONs surface did not influence the iron oxide core size, maintaining the particle diameter between 8–10 nm, in concordance with the average crystallite size obtained from the XRD analysis. TEM analysis after RhoB functionalization was also performed to verify possible influences on SPIONs morphology and size distribution (Supplementary Information, figure S1B). It is observable that the morphology and mean diameter, equal to 9 ± 2 nm, are maintained within the superparamagnetic behavior range.

Magnetic measurements were performed to evaluate the effect of APTES coating on the magnetic properties of SPIONs. Figure 1(D) shows the hysteresis curves at 5 K and 300 K. At 300 K, the sample is superparamagnetic, as demonstrated by the absence of coercivity and remanence (inset of figure 1(D)). The saturation magnetization at 300 K is 52 $emu.g^{-1}$, which is reduced compared to base SPIONs. This reduction is caused by the coating material, as previously demonstrated [31, 36, 39].

3.2. Protein corona formation

When nanoparticles are in contact with the physiological environment, large amounts of protein may adsorb at its surface, forming a protein corona [40–42]. Table 1 shows the zeta potential, Dh, and polydispersity index (PDI) of SPIONs coated with APTES without and functionalized with RhoB. The zeta potential values show that SPIONs_APTES in water exhibit a positive surface charge with values associated with NPs stability. When the NPs are resuspended in PBS or cell culture medium, the value decays to a zeta potential close to neutral. As the difference in charge may affect the particles' stability, an evident increase of Dh and polydispersity index (table 1) associated with higher decay times in the autocorrelation curve (figure S2—Supplementary information) was observable. It is visible that all samples in water, except SPIONs_APTES, have higher decay times, corresponding to the high Dh obtained. In SPIONs_APTES in water, the decay time is significantly reduced, although two decays may be identified. The first one (with a shorter delay time) corresponds to particles with smaller sizes, and the second one (with a longer decay time) to particle aggregates. No significant differences were observed with the presence of serum (FBS). DLS measurements were also performed in DMEM with 10% and 0% FBS. Typically, a correlation curve starts at 1 due to the similarity between the scattered patterns at the initial seconds of the measurement. The DMEM 10% FBS correlation curve starts at 0.6 ($\ll$1), resulting in smaller hydrodynamic sizes after data analysis. This could be justified by a rapid sedimentation of serum proteins, leaving a small quantity of dispersed proteins to scatter the light. The significant increase in Dh may be related to the positive charge of APTES, leading to high adsorption of proteins with a negative charge present in the cell culture medium, as demonstrated in previous studies [41, 43].

SPIONs_APTES functionalized with RhoB were also analyzed to evaluate the effect of RhoB on protein corona formation. In water, the zeta potential value decreases to a negative one. This may be associated with the presence of RhoB, leading to a negative surface charge [44]. However, the low value (−14 ± 2 mV) is not within

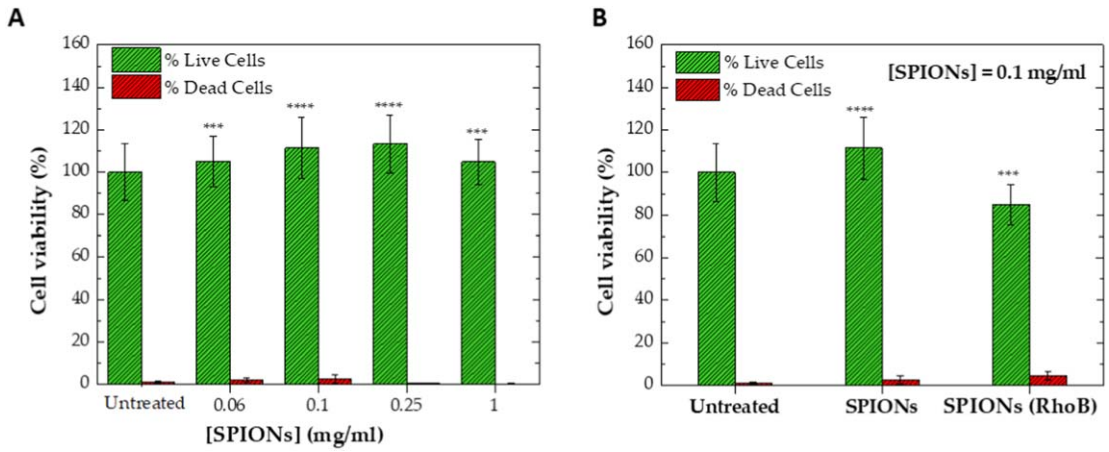

Figure 2. Live/Dead cell viability assay of SPIONs_APTES and SPIONs_APTES (RhoB) towards WM983b melanoma cell line. Percentage of live and dead cells after 24 h exposure with (A) 0.06 to 1 mg ml^{-1} of SPIONs_APTES and (B) 0.1 mg ml^{-1} of SPIONs_APTES (RhoB) compared with the same selected concentration of SPIONs_APTES. **** p-value < 0.0001 *** p-value < 0.001 relative to control of untreated cells. Data is expressed as mean percentage of live and dead cells (in bars) $\pm$ SD (vertical error bars). At least 15 images were taken at 10 $\times$ magnification in random areas of 3 different wells per condition. Images were analyzed using Cell Profiler software to count the number of cells per image discriminated by morphology and fluorescence intensity parameters in the green and red channels.

the range considered for stability, which is confirmed by the high Dh and PDI, probably caused by NPs aggregates. When SPIONs_RhoB are dispersed in a cell culture medium, although the Dh and PDI are slightly smaller than non-functionalized SPIONs_APTES, they are still too large, thus confirming protein corona formation. Therefore, the presence of RhoB at the surface of NPs does not prevent the formation of the protein corona.

3.3. WM983b melanoma cell line response to SPIONs

Live/Dead assay confirmed the non-cytotoxic effect of SPIONs in the WM983b cell line after 24 h exposure, with a high percentage of live cells and a maximum of 3% of dead cells (figure 2(A)). Any toxicity was discarded for the concentration of 0.1 mg ml^{-1} of SPIONs_APTES and RhoB functionalized SPIONs (figure 2(B)).

Prussian blue staining images of SPIONs interaction with WM983b melanoma cell line in single-cell suspension, cell monolayer (2D model), and spheroid (3D model) show SPIONs localization after 1 h, 6 h, and 24 h of exposure to a concentration of 0.1 mg ml^{-1} of SPIONs compared with untreated condition (figure 3). The transmitted light images concerning all the mentioned incubation periods are in Supplementary Information, figure S3.

A qualitative analysis of the images indicates a rapid interaction of SPIONs with the cell membrane, similar to either in single-cell suspension or cell monolayer. For the spheroid model, this occurs later on and is possibly associated with the close interaction of cells, creating physical barriers and reducing the accessibility of nanoparticle-binding sites on cell surfaces. For long periods of exposure, the higher predominance of blue in Prussian blue images is evidence of an increase of SPIONs either strongly attached to the cell membrane or already internalized.

In cell monolayer, a quantitative measurement of internalization over time by flow cytometry reveals that the maximum internalization is reached after 6 h of SPIONs exposure (figure 4(A)). Confocal microscopy images (figure 4(B)) give a more detailed representation of SPIONs internalization profile. As the incubation period increases, the accumulation of SPIONs around the cell nucleus becomes more pronounced after 6 h of incubation, which, for longer periods, is less evident, consistent with the findings from flow cytometry.

3.4. SMI efficiency in inhibiting SPIONs uptake

Possible cytotoxicity of CPZ, genistein, latrunculin B, nocodazole, and MβCD at the selected concentrations was discarded with a resazurin cell viability assay (Supplementary Information, figure S4). In figure 5(A), confocal microscopy images reveal pronounced differences in SPIONs uptake for each SMI compared with untreated cells. By observation, MβCD and nocodazole show a lower prevalence of SPIONs inside the cell cytoplasm. Given the marked differences between conditions, image processing of the acquired images was used to profile SPIONs distribution in the cell's area considered (figure 5(B)). It is notorious that, for all conditions, there is a higher accumulation of SPIONs around the cell nucleus, which reduces as the distance increases. Also, a pre-treatment with any SMI leads to a lower predominance of SPIONs inside the cells, compared with untreated

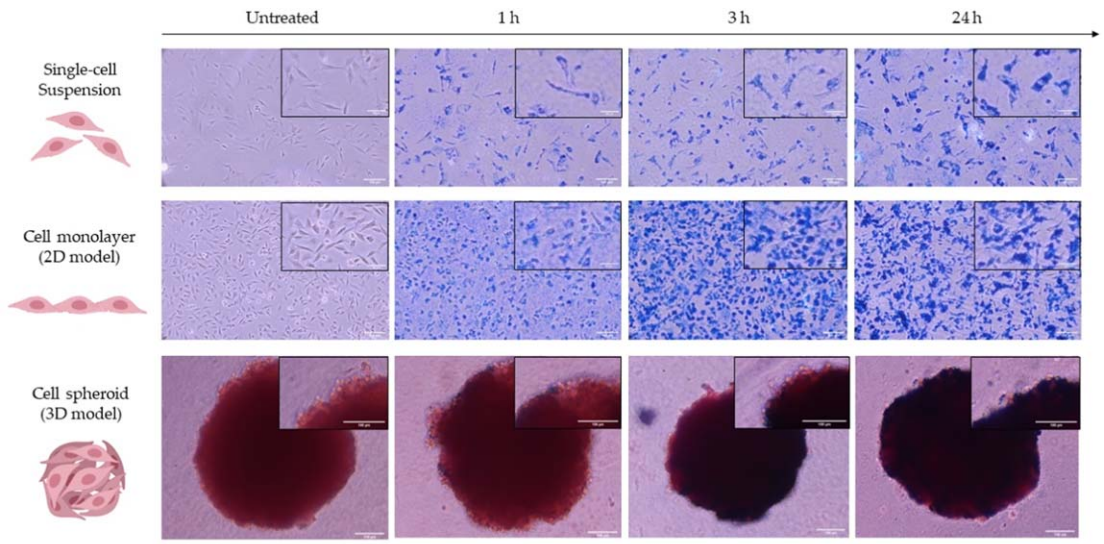

Figure 3. Prussian blue staining showing SPIONs intracellular localization in WM983b melanoma cells in single-cell suspension, cell monolayer, and spheroids after 1 h, 3 h, and 24 h treatment with 100 μg ml^{-1} of SPIONs. Untreated conditions for all models are also shown for comparison. Bright field images with 20 × objective magnification with scale bar: 100 μm and respective amplifications in representative areas with scale bar: 50 μm.

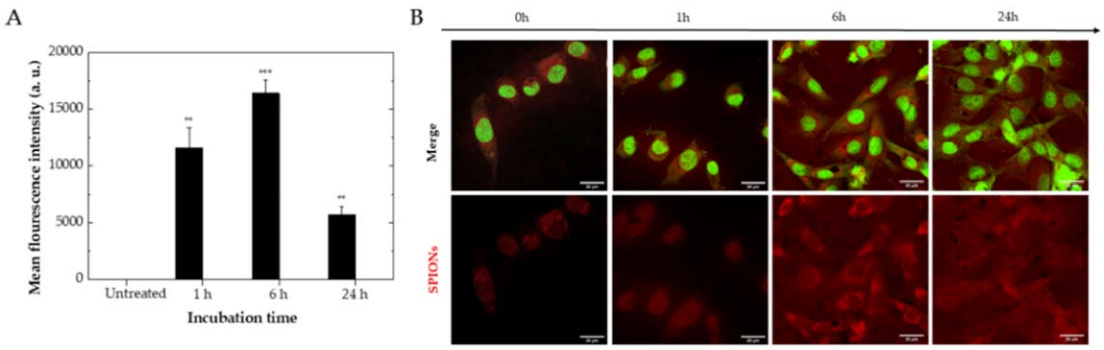

Figure 4. Flow cytometry and Confocal microscopy of SPIONs uptake over time. (A) Flow cytometry analysis of SPIONs (RhoB) internalization in WM983b melanoma cell line after 1 h, 6 h, and 24 h incubation compared with control of untreated cells. (B) Representative images of confocal fluorescence microscopy of SPIONs (RhoB). Images from red channel (SPIONs conjugated with RhoB fluorophore) and merge of red and green channel (cell nuclei and actin filaments staining with helix-green and phalloidin-488 dyes), acquired with Zeiss LSM700 microscope with 20 × objective. Scale bar: 20 μm. *** p-value < 0.001, ** p-value < 0.01 relative to control of untreated cells.

control. From around 40 μm distance from the cell end, a stabilization of the fluorescence intensity was verified, translating into an even distribution of SPIONs over the cell cytoplasm. This distribution profile is not observed for untreated conditions, with a high predominance of SPIONs over all the cell areas.

The area of SPIONs distribution profile corresponding to each condition was calculated and translated into cellular uptake of SPIONs per cell. Figure 5(C) demonstrates an average maximum 60% of cellular uptake in the presence of SMI, indicating that all may affect cell components involved in SPIONs transport. In the case of MβCD, the red fluorescence intensity is the lowest for the considered cell area, significantly reducing SPIONs uptake to only 14%. These findings were validated using flow cytometry analysis (figure 5(D)), which confirmed significant inhibitory action of MβCD in SPIONs internalization at the internalization peak of 6 h. However, over a prolonged incubation period of 24 h, the influence of MβCD appeared to be not significant. Based on the MβCD mechanism of action, this may be attributed to the cells' ability to overcome the cholesterol depletion effect within this timeframe.

3.5. Magnetic hyperthermia assays

Magnetic hyperthermia therapy promotes cancer cell death by apoptosis due to the higher sensitivity of cancer cells to temperature oscillations around 42 °C [45]. SPIONs heating curves for 1 mg ml^{-1}, 2 mg ml^{-1}, and

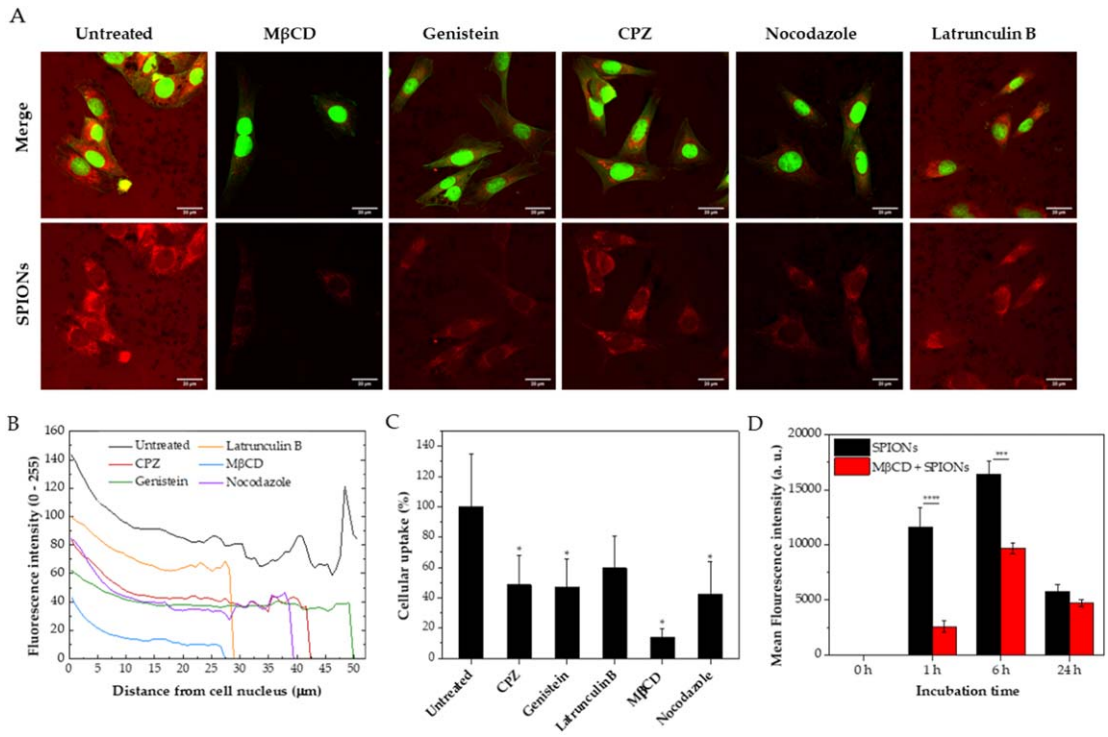

Figure 5. Uptake studies of SPIONs in WM983b melanoma cell line. (A) Confocal microscopy images of untreated and treated conditions with 5 mM MβCD, 25 μM genistein, 5 μM CPZ, 10 μM nocodazole, and 10 μM latrunculin B. Images from green channel (cell nuclei and actin filaments staining with helix-green and phalloidin-488 dyes), red channel (SPIONs conjugated with RhoB fluorophore) and merge of both channels, acquired with Zeiss LSM 700 microscope with 20 × objective. Scale bar: 20 μm. (B) Graphical representation of SPIONs distribution profile over the cell area. Considering 3-pixel width contours, from the nucleus to the cell end, an average of red channel fluorescence intensity for each contour was calculated for at least 20 individual cells per condition and represented in RGB values (0–255). Pixel was converted into μm according to the image scale bar. (C) Cellular uptake of SPIONs calculated from the area of SPIONs distribution profile for each individual cell. Data is expressed as mean percentage of at least 20 individual cells per condition normalized to control (cells exposed to the nanoparticles but untreated with SMI). (D) Flow cytometry analysis of SPIONs uptake in WM983b melanoma cell line after 1 h, 6 h, and 24 h incubation, with and without pre-treatment with 5 mM MβCD, normalized to untreated control (0 h). ****p-value < 0.0001 ***p-value < 0.001, **p-value < 0.01 relative to control.

3.5 mg ml^{-1} concentrations (Supplementary Information, figure S5A) represent the temperature increase as a function of the exposure time to the AMF. The results show that temperature values increase for higher concentrations of SPIONs in solution. For this study, we selected 3.5 mg ml^{-1} SPIONs concentration, reaching 42 °C after 5 min under the AMF.

Before performing *in vitro* studies, the influence of cell culture conditions on the SPIONs heat dissipation was evaluated (Supplementary Information, figures S5(B), S5(C)). No relevant differences in temperature increase normalized to SPIONs concentration were observed between water and supplemented cell culture medium. These results may be explained by the presence of APTES at the surface of iron oxide nanoparticles. Typically, superparamagnetic iron oxide nanoparticles produce heat under an external AMF due to Brownian and Néel relaxation mechanisms. If one considers the uptake of NPs by tumor cells in *in vivo* conditions, the Néel relaxation mechanism is more significant since it may occur even if the NPs are entrapped within the tumor [46]. As previously demonstrated [14], the surfactant may also significantly reduce the Brownian relaxation mechanism, thus leading to heat generation mainly by the Néel relaxation mechanism. Therefore, when protein corona is formed, generating particles with high Dh, the generated heat is similar since the Brownian relaxation mechanisms were already suppressed by the surfactant, in this case, APTES [47].

The heating efficiency of the magnetic material was also calculated from the magnetic hyperthermia measurements. This efficiency is given by SAR and calculated using the following equation:

$$SAR(W/g) = \frac{C_{NP}\, m_{Fe} + C_l m_l}{m_{Fe}} \left(\frac{dT}{dt}\right)_{\max} \quad (1)$$

where $(dT/dt)_{max}$ is the maximum slope of the temperature curve ensuring adiabatic conditions, C_{NP} is the specific heat of SPIONs, C_l is the specific heat of the liquid, m_l is the fluid mass, and m_{Fe} is the iron mass of the sample. The SAR value for SPIONs in water is 160 ± 19 W g^{-1}, similar to 156 ± 9 W g^{-1} in DMEM with 10%

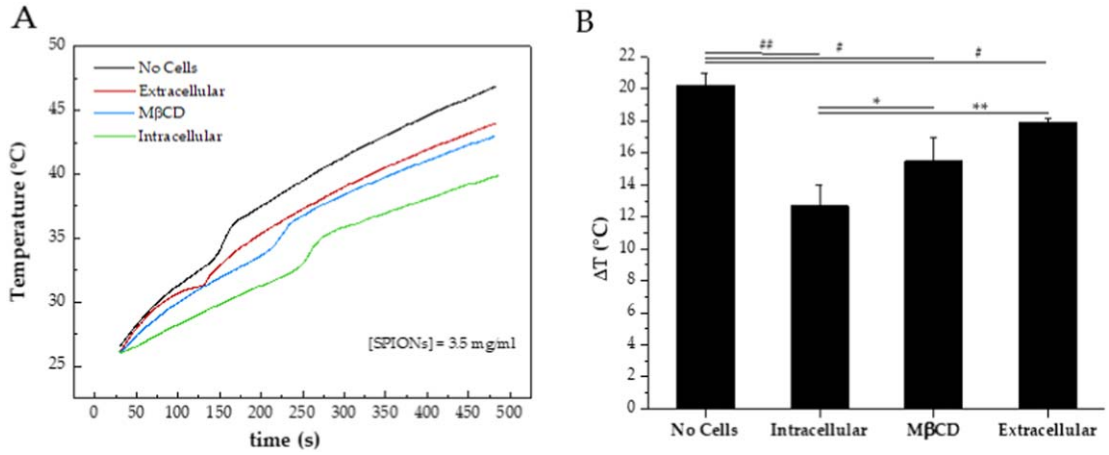

Figure 6. *In vitro* magnetic hyperthermia assay. (A) Temperature curve of SPIONs in response to an AMF application with intensity of 300 G at a frequency of 418.5 kHz, for 8 min, for all conditions. (B) SAR values reflecting SPIONs heating capacity, for all conditions. Data is expressed as mean ± SD for at least three measurements. ##p-value < 0.01, #p-value < 0.05 relative to no cells condition; **p-value < 0.01, *p-value < 0.05 relative to intracellular magnetic hyperthermia condition.

FBS condition. These values are within the expected range for magnetic hyperthermia application [14], demonstrating the potential of the developed magnetic colloid.

For *in vitro* magnetic hyperthermia studies, the effect of SPIONs uptake inhibition by MβCD in temperature increase was compared against intracellular and extracellular controls and the SPIONs suspension without any cells (figure 6). Temperature curves (figure 6(A)) show that the presence of cells in the suspension affects SPIONs heat dissipation over exposure to the AMF. Comparing between uptake conditions, our results evidence that the temperature increase is notably lower when SPIONs are intracellularly ($\Delta T = 12.9 \pm 1.3$ °C) compared to extracellular control ($\Delta T = 18.0 \pm 0.2$ °C), thus validating our initial premise. Inhibiting SPIONs uptake with MβCD significantly improved temperature increase to $\Delta T = 15.5 \pm 1.5$ °C, confirming our hypothesis. For all conditions, SAR values were determined (figure 6(B)), reflecting these findings showing lower SPIONs heating capacity for intracellular control (63 ± 7 W g^{-1}), which increases after cellular uptake blockade (91 ± 16 W g^{-1}), comparable with extracellular control (108 ± 19 W g^{-1}).

4. Discussion

Magnetic hyperthermia has been explored over the years as an alternative cancer therapy. Using SPIONs to generate heat at the tumor site, malignant cells die due to high susceptibility to temperature increases. More recently, studies have revealed that SPION's heating capacity is impaired when internalized by cancer cells due to their lack of mobility and, as a consequence, the lack of Brownian relaxation [46]. Our hypothesis is based on using small molecule inhibitors (SMIs) of endocytosis to inhibit the uptake of SPIONs, thereby potentially improving magnetic hyperthermia therapy efficiency, to be applied for advanced cutaneous melanoma.

Our work involved synthesizing spherical stabilized magnetic nanoparticles with a diameter within the superparamagnetic behavior range and a positive surface charge. Given that protein corona formation influences the cellular uptake pathway of nanoparticles, we evaluated the stability of the produced SPIONs in the presence and absence of serum proteins [41]. As demonstrated by previous studies, positively charged nanoparticles increase protein adsorption to their surfaces via electrostatic interactions, given that most proteins are negatively charged. This phenomenon alters ζ-potential from positive to neutral in the cell culture medium, aligning with our results [41, 42]. A neutral surface charge is associated with nanoparticles' loss of stability in aqueous solutions and the formation of aggregates. Our hydrodynamic diameter and polydispersity index results confirm this observation, evidencing the formation of a protein corona around SPIONs surface. Although Dh may be an indication of NP aggregation, it may also just reflect the formation of protein corona around the NP. Therefore, additional quantitative studies could confirm this hypothesis, together with morphological analysis. Particularly because large aggregates usually affect cell uptake, primarily through endocytosis. Positively charged nanoparticles have a higher rate of cell internalization [29, 41, 48]. Our uptake studies in WM983b melanoma cell line suggest that the internalization process may start with a rapid interaction between the melanoma cell membrane and SPIONs surface, followed by a mechanism of uptake with SPIONs accumulation around the cell nucleus within 6 h incubation, as observed by others [49].

To enhance magnetic hyperthermia efficiency as a therapeutic option for advanced melanoma, we performed a treatment with a selection of SMI of endocytosis and conducted *in vitro* uptake studies of SPIONs. Our results indicate a decrease in internalization to a maximum 60%, compared to untreated cells, in the presence of the selected SMI, indicating that all may affect cell components involved in SPIONs transport. Pre-treatment with 5 mM of MβCD had a higher inhibitory effect. MβCD mechanism of action consists of cholesterol depletion from the cell membrane, which, considering our findings, may affect SPIONs internalization in WM983b melanoma cell line. As such, the uptake route could be associated with the caveolin-mediated endocytic pathway, although some argue that multiple pathways are affected [50, 51].

According to our *in vitro* magnetic hyperthermia measurements, the internalization of SPIONs highly affects their heat dissipation compared to the extracellular control. This has also been observed by Hannon *et al* [23] for pancreatic adenocarcinoma. The initial hypothesis was confirmed, as our results demonstrate that blocking SPIONs uptake with MβCD translates into a significant temperature increase of the solution, reflected in SPIONs SAR value. Further investigation is needed regarding the effect on cell viability and towards an efficient alternative to current melanoma therapeutic approaches.

5. Conclusions

Our study aimed to improve magnetic hyperthermia treatment for advanced cutaneous melanoma cells by inhibiting the cellular uptake of SPIONs using SMI of endocytosis. Among the panel of inhibitors studied, our results indicate that MβCD effectively impairs SPIONs' uptake in an advanced cutaneous melanoma cell line. This improves SPIONs' heat dissipation capacity and increases temperature under *in vitro* magnetic hyperthermia conditions. Our findings reveal that SMI can be used to modulate nanoparticle internalization, which opens new possibilities for developing nanoparticle-based therapeutics. Additionally, it contributes to improving magnetic hyperthermia therapy and, consequently, therapeutic outcomes for cancer patients. To our knowledge, this is the first report on preventing the cellular uptake of magnetic nanoparticles to improve melanoma magnetic hyperthermia cancer treatment efficiency.

Acknowledgments

This work was financed by FCT—Portuguese Foundation for Science and Technology, in the framework of the project PTDC/BTM-MAT/2472/2021 and projects LA/P/0037/2020, UIDP/50025/2020 and UIDB/50025/2020 of the Associate Laboratory Institute of Nanostructures, Nanomodelling and Nanofabrication-i3N. C.I.P.C. is supported by the grant SFRH/BD/148588/2019 from the Portuguese Foundation for Science and Technology (FCT).

Data availability statement

This data is a part of an ongoing PhD project, and will be made available once the work is complete. The data that support the findings of this study are available upon reasonable request from the authors.

Authorship contribution

Conception and design of study: BS, FA, PS; Acquisition of data: BS, CC, MAV, MCC, FA. Data analysis and/or interpretation: BS, CC, TV, MCC, FA, PS. Drafting of the manuscript: BS; Review and editing: CC, TV, MCC, VN, JS, JPB, FA, PS. Supervision: FA, PS. Funding acquisition: JPB, PS, VN.

Availability of data and materials

The datasets supporting the conclusions of this article are included within the article and its additional files.

ORCID iDs

Beatriz T Simões https://orcid.org/0000-0001-7880-7718
Catarina Chaparro https://orcid.org/0000-0002-4030-2519
Marco C V Cavaco https://orcid.org/0000-0002-0938-9038

João Paulo Borges https://orcid.org/0000-0002-3996-6545
Paula Soares https://orcid.org/0000-0002-4975-7480

References

[1] Sung H, Ferlay J, Siegel R L, Laversanne M, Soerjomataram I, Jemal A and Bray F 2021 Global cancer statistics 2020: GLOBOCAN estimates of incidence and mortality worldwide for 36 cancers in 185 countries *CA Cancer J. Clin.* **71** 209–49
[2] Arnold M, Singh D, Laversanne M, Vignat J, Vaccarella S, Meheus F, Cust A E, de Vries E, Whiteman D C and Bray F 2022 Global burden of cutaneous melanoma in 2020 and projections to 2040 *JAMA Dermatology* **158** 495–503
[3] Globocan 2022 https://gco.iarc.fr/IARC
[4] Yuan T A, Lu Y, Edwards K, Jakowatz J, Meyskens F L and Liu-Smith F 2019 Race-, age-, and anatomic site-specific gender differences in cutaneous melanoma suggest differential mechanisms of early- and late-onset melanoma *International Journal of Environmental Research and Public Health* **16** 908
[5] Lo J A and Fisher D E 2014 The melanoma revolution: from UV carcinogenesis to a new era in therapeutics *Science* **346** 945–9
[6] Zhang J, Joshua A M, Li Y, O'Meara C H, Morris M J and Khachigian L M 2024 Targeted therapy, immunotherapy, and small molecules and peptidomimetics as emerging immunoregulatory agents for melanoma *Cancer Lett* **586** 216633
[7] Albrecht L J *et al* 2024 Anti-PD-(L)1 plus BRAF/MEK inhibitors (triplet therapy) after failure of immune checkpoint inhibition and targeted therapy in patients with advanced melanoma *European Journal of Cancer* **202** 113976
[8] Pasquali S, Hadjinicolaou A V, Chiarion Sileni V, Rossi C R and Mocellin S 2018 Systemic treatments for metastatic cutaneous melanoma *The Cochrane Database of Systematic Reviews* **2** Cd011123
[9] Almeida F V, Douglass S M, Fane M E and Weeraratna A T 2019 Bad company: microenvironmentally mediated resistance to targeted therapy in melanoma *Pigment Cell & Melanoma Research* **32** 237–47
[10] Sadrolashrafi K and Samlowski W 2023 Retreatment of patients with metastatic cutaneous melanoma who relapse after elective checkpoint inhibitor discontinuation after a complete remission *Oncologist* **28** e270–5
[11] Ng G, Xu W and Atkinson V 2022 Treatment approaches for melanomas that relapse after adjuvant or neoadjuvant therapy *Curr. Oncol. Rep.* **24** 1273–80
[12] Gorry C, McCullagh L, O'Donnell H, Barrett S, Schmitz S, Barry M, Curtin K, Beausang E, Barry R and Coyne I 2023 Neoadjuvant treatment for stage III and IV cutaneous melanoma *The Cochrane Database of Systematic Reviews* **1** Cd012974
[13] Soares P I P, Romão J, Matos R, Silva J C and Borges J P 2021 Design and engineering of magneto-responsive devices for cancer theranostics: nano to macro perspective *Prog. Mater Sci.* **116** 100742
[14] Soares P I P, Laia C A T, Carvalho A, Pereira L C J, Coutinho J T, Ferreira I M M, Novo C M M and Borges J P 2016 Iron oxide nanoparticles stabilized with a bilayer of oleic acid for magnetic hyperthermia and MRI applications *Appl. Surf. Sci.* **383** 240–7
[15] Chaparro C I P, Simoes B T, Borges J P, Castanho M, Soares P I P and Neves V 2023 A promising approach: magnetic nanosystems for alzheimer's disease theranostics *Pharmaceutics* **15** 2316
[16] Etemadi H and Plieger P G 2020 Magnetic fluid hyperthermia based on magnetic nanoparticles: physical characteristics, historical perspective, clinical trials, technological challenges, and recent advances *Advanced Therapeutics* **3** 2000061
[17] Patil R M, Thorat N D, Shete P B, Bedge P A, Gavde S, Joshi M G, Tofail S A M and Bohara R A 2018 Comprehensive cytotoxicity studies of superparamagnetic iron oxide nanoparticles *Biochemistry and Biophysics Reports* **13** 63–72
[18] Lee S Y, Fiorentini G, Szasz A M, Szigeti G, Szasz A and Minnaar C A 2020 Quo vadis oncological hyperthermia (2020)? *Frontiers in Oncology* **10** 1690
[19] Obaidat I M, Narayanaswamy V, Alaabed S, Sambasivam S and Muralee Gopi C V V 2019 Principles of magnetic hyperthermia: a focus on using multifunctional hybrid magnetic nanoparticles *Magnetochemistry* **5** 67
[20] Cabrera D, Coene A, Leliaert J, Artés-Ibáñez E J, Dupré L, Telling N D and Teran F J 2018 Dynamical magnetic response of iron oxide nanoparticles inside live cells *ACS Nano* **12** 2741–52
[21] Beola L *et al* 2020 The intracellular number of magnetic nanoparticles modulates the apoptotic death pathway after magnetic hyperthermia treatment *ACS Appl. Mater. Interfaces* **12** 43474–87
[22] Beola L, Asín L, Fratila R M, Herrero V, de la Fuente J M, Grazú V and Gutiérrez L 2018 Dual role of magnetic nanoparticles as intracellular hotspots and extracellular matrix disruptors triggered by magnetic hyperthermia in 3D cell culture models *ACS Appl. Mater. Interfaces* **10** 44301–13
[23] Hannon G, Bogdanska A, Volkov Y and Prina-Mello A 2020 Comparing the effects of intracellular and extracellular magnetic hyperthermia on the viability of BxPC-3 Cells *Nanomaterials (Basel, Switzerland)* **10** 593
[24] Laurent S, Dutz S, Hafeli U O and Mahmoudi M 2011 Magnetic fluid hyperthermia: focus on superparamagnetic iron oxide nanoparticles *Adv. Colloid Interface Sci.* **166** 8–23
[25] Soukup D, Moise S, Céspedes E, Dobson J and Telling N D 2015 *In situ* measurement of magnetization relaxation of internalized nanoparticles in live cells *ACS Nano* **9** 231–40
[26] Manzanares D and Ceña V 2020 Endocytosis: the nanoparticle and submicron nanocompounds gateway into the cell *Pharmaceutics* **12** 371
[27] Gan B K, Yong C Y, Ho K L, Omar A R, Alitheen N B and Tan W S 2018 Targeted delivery of cell penetrating peptide virus-like nanoparticles to skin cancer cells *Sci. Rep.* **8** 8499
[28] Dutta D and Donaldson J G 2012 Search for inhibitors of endocytosis: intended specificity and unintended consequences *Cellular Logistics* **2** 203–8
[29] Behzadi S, Serpooshan V, Tao W, Hamaly M A, Alkawareek M Y, Dreaden E C, Brown D, Alkilany A M, Farokhzad O C and Mahmoudi M 2017 Cellular uptake of nanoparticles: journey inside the cell *Chem. Soc. Rev.* **46** 4218–44
[30] Chen L, Wang H, Li X, Nie C, Liang T, Xie F, Liu K, Peng X and Xie J 2018 Highly hydrophilic carbon nanoparticles: uptake mechanism by mammalian and plant cells *RSC Adv.* **8** 35246–56
[31] Soares P I, Alves A M, Pereira L C, Coutinho J T, Ferreira I M, Novo C M and Borges J P 2014 Effects of surfactants on the magnetic properties of iron oxide colloids *J. Colloid Interface Sci.* **419** 46–51
[32] Mashhadizadeh M H and Amoli-Diva M 2012 Drug-carrying amino silane coated magnetic nanoparticles as potential vehicles for delivery of antibiotics *Journal of Nanomedicine & Nanotechnology* **03** 139
[33] Talelli M, Rijcken C J, Lammers T, Seevinck P R, Storm G, van Nostrum C F and Hennink W E 2009 Superparamagnetic iron oxide nanoparticles encapsulated in biodegradable thermosensitive polymeric micelles: toward a targeted nanomedicine suitable for image-guided drug delivery *Langmuir* **25** 2060–7

[34] Schneider C A, Rasband W S and Eliceiri K W 2012 NIH image to Imagej: 25 years of image analysis *Nat. Methods* **9** 671–5
[35] Michael Economo 2019 Mowiol mounting media. protocols.io (https://org/10.17504/protocols.io.8p6hvre)
[36] Soares P I, Lochte F, Echeverria C, Pereira L C, Coutinho J T, Ferreira I M, Novo C M and Borges J P 2015 Thermal and magnetic properties of iron oxide colloids: influence of surfactants *Nanotechnology* **26** 425704
[37] Bayat A, Shakourian-Fard M, Ehyaei N and Hashemi M M 2014 A magnetic supported iron complex for selective oxidation of sulfides to sulfoxides using 30% hydrogen peroxide at room temperature *RSC Adv.* **4** 44274–81
[38] Wu W, Wu Z, Yu T, Jiang C and Kim W-S 2015 Recent progress on magnetic iron oxide nanoparticles: synthesis, surface functional strategies and biomedical applications *Sci. Technol. Adv. Mater.* **16** 023501
[39] Matos R J R, Chaparro C I P, Silva J C, Valente M A, Borges J P and Soares P I P 2018 Electrospun composite cellulose acetate/iron oxide nanoparticles non-woven membranes for magnetic hyperthermia applications *Carbohydr Polym* **198** 9–16
[40] Lundqvist M, Stigler J, Elia G, Lynch I, Cedervall T and Dawson K A 2008 Nanoparticle size and surface properties determine the protein corona with possible implications for biological impacts *Proc. Natl Acad. Sci.* **105** 14265–70
[41] Calatayud M P, Sanz B, Raffa V, Riggio C, Ibarra M R and Goya G F 2014 The effect of surface charge of functionalized Fe3O4 nanoparticles on protein adsorption and cell uptake *Biomaterials* **35** 6389–99
[42] Wolfram J, Yang Y, Shen J, Moten A, Chen C, Shen H, Ferrari M and Zhao Y 2014 The nano-plasma interface: implications of the protein corona *Colloids Surf B Biointerfaces* **124** 17–24
[43] Portilla Y, Mellid S, Paradela A, Ramos-Fernández A, Daviu N, Sanz-Ortega L, Pérez-Yagüe S, Morales M P and Barber D F 2021 Iron oxide nanoparticle coatings dictate cell outcomes despite the influence of protein coronas *ACS Appl. Mater. Interfaces* **13** 7924–44
[44] Yu Y, Murthy B N, Shapter J G, Constantopoulos K T, Voelcker N H and Ellis A V 2013 Benzene carboxylic acid derivatized graphene oxide nanosheets on natural zeolites as effective adsorbents for cationic dye removal *J. Hazard. Mater.* **260** 330–8
[45] Jindal A, Sarkar S and Alam A 2021 Nanomaterials-mediated immunomodulation for cancer therapeutics *Frontiers in Chemistry* **9** 629635
[46] Liu X, Kaminski M D, Guan Y, Chen H, Liu H and Rosengart A J 2006 Preparation and characterization of hydrophobic superparamagnetic magnetite gel *J. Magn. Magn. Mater.* **306** 248–53
[47] Lima E, De Biasi E, Zysler R D, Vasquez Mansilla M, Mojica-Pisciotti M L, Torres T E, Calatayud M P, Marquina C, Ricardo Ibarra M and Goya G F 2014 Relaxation time diagram for identifying heat generation mechanisms in magnetic fluid hyperthermia *J. Nanopart. Res.* **16** 1–11
[48] Zhang D, Wei L, Zhong M, Xiao L, Li H-W and Wang J 2018 The morphology and surface charge-dependent cellular uptake efficiency of upconversion nanostructures revealed by single-particle optical microscopy *Chem. Sci.* **9** 5260–9
[49] Liang R *et al* 2013 Multifunctional biodegradable polymer nanoparticles with uniform sizes: generation and *in vitro* anti-melanoma activity *Nanotechnology* **24** 455302
[50] Francia V, Reker-Smit C, Boel G and Salvati A 2019 Limits and challenges in using transport inhibitors to characterize how nano-sized drug carriers enter cells *Nanomedicine (Lond)* **14** 1533–49
[51] Iversen T-G, Skotland T and Sandvig K 2011 Endocytosis and intracellular transport of nanoparticles: present knowledge and need for future studies *Nano Today* **6** 176–85